Relaxation Processes of Translationally Hot O(^{1}D) by Collisions with O_2

Nori Taniguchi, Kouichi Hirai, Kenshi Takahashi, and Yutaka Matsumi*

Solar-Terrestrial Environment Laboratory and Graduate School of Science, Nagoya University, 3-13, Honohara, Toyokawa 442-8507, Japan

Received: December 7, 1999; In Final Form: February 9, 2000

The collisions of translationally hot O(^{1}D) with O_2 result in two processes, translational energy relaxation and electronic quenching to O(^{3}P). These two processes were studied in a gas cell at room temperature using the vacuum ultraviolet laser-induced fluorescence technique. The initial hot O(^{1}D) atoms were produced by the photodissociation of N_2O at 193 nm, which have average translational energies of 18.1 kcal mol^{-1} in the laboratory frame. Time-resolved measurements of the Doppler profiles for the hot O(^{1}D) atoms revealed the translational energy relaxation process, whereas the quenching process was investigated by measuring both the decrease of the O(^{1}D) concentration and the increase of the product O(^{3}P) concentration at various delay times after the photochemical formation of the hot O(^{1}D) atoms. From the simulation employing an elastic hard-sphere collision model with a Monte Carlo method, the hard-sphere diameter for the translational energy relaxation process of hot O(^{1}D) by collisions with O_2 was found to be 2.5 ± 0.2 Å. The cross section of the electronic quenching of O(^{1}D) by O_2 at the high collision energy of 8.7 ± 6 kcal mol^{-1} was found to be 3.3 ± 0.7 Å^2, which is a little smaller than that at the thermal collision energy at 298 K. The observed collision energy dependence is explained by a centrifugal barrier on the entrance attractive potential surface of the quenching reaction.

1. Introduction

The role of energetic atoms in the heat and energy balance of the upper atmosphere is an important aspect of atmospheric chemistry. It has been considered that the chemical reactions in the Earth's atmosphere proceed under conditions of local thermodynamic equilibrium. However, in the upper atmosphere, O(^{1}D) atoms generated by the photodissociation of O_2 and O_3 molecules by the sunlight in the ultraviolet (UV) and vacuum ultraviolet (VUV) region have large kinetic energies.[1] This is because a part of the excess energy of the photodissociation reaction is released into the kinetic energy of the photofragments. Their energy is redistributed to the surrounding atmospheric bath gases through elastic and inelastic collisions. Matsumi and Chowdhury[2] reported that the translational energy relaxation rate of translationally hot O(^{1}D) by collisions with N_2 is not fast enough compared with the electronic quenching rate. They indicated that the populations of O(^{1}D) at the high translational energies in the steady-state condition in the atmosphere are larger than the Boltzmann distribution at the local temperature.

In this paper, we report the investigation of the two competitive collisional processes 1 and 2 of the translationally hot O(^{1}D) atoms with O_2:

$$\text{Fast } O(^1D) + O_2 \rightarrow \text{slow } O(^1D) + O_2 \qquad \text{translational energy relaxation} \quad (1)$$

$$O(^1D) + O_2 \rightarrow O(^3P_j) + O_2 \qquad \text{electronic quenching} \quad (2)$$

In the studies on the translational energy relaxation of hot atoms,[2−5] Doppler profiles of initially energetic atoms moving in different bath gases were measured as a function of time, and effective hard-sphere model cross sections were derived for translational energy and angular relaxation. The measurements of the collisional relaxations of energetic O(^{1}D) atoms produced in the photolysis of O_2 and N_2O were reported by Matsumi et al.[2,5] Their experimental results for the relaxation processes by collisions with monatomic[5] and diatomic molecule[2] bath gases were well reproduced by their Monte Carlo simulations with an elastic hard-sphere collision model. Tachikawa et al.[6] calculated ab initio potential surfaces for the O(^{1}D) + N_2 collision system, and they performed classical trajectory surface hopping calculations[7] to determine the efficiency of translational energy relaxation versus electronic quenching. Quantum mechanical calculations for the thermalization of initially hot O(^{1}D) atoms in a bath gas of N_2 molecules were carried out by Balakrishnan et al.[8] They presented quantum mechanical calculations of the translational energy and angular dependence of collision cross sections to predict the translational energy relaxation as a function of time. Their results on the translational energy relaxation of hot O(^{1}D) atoms were in good agreement with the experimental results of Matsumi et al.[2,5] They concluded that the energy losses arise predominantly from elastic scattering, with a small contribution from inelastic rotational and vibrational excitation.

The NASA/JPL[9] has recommended the rate constant of the electronic quenching process 2 of 4.0 × 10^{-11} cm^3 molecule^{-1} s^{-1} at 298 K, with 3.2 × 10^{-11} exp[(70 ± 100)/T] for the temperature dependence. The latter is based on the measurements between 104 and 354 K by Streit et al.[10] The electronic energy of the O(^{1}D) atom is 1.97 eV and is sufficiently high to form the following three possible excited molecular products:

* Corresponding author. Fax: +81-533-89-5593. E-mail: matsumi@stelab.nagoya-u.ac.jp.

10.1021/jp994291d CCC: $19.00
Published on Web 04/05/2000

$$O(^1D) + O_2(X^3\Sigma_g^-) \rightarrow O(^3P) + O_2(b^1\Sigma_g^+) \quad (2a)$$

$$\rightarrow O(^3P) + O_2(a^1\Delta_g) \quad (2b)$$

$$\rightarrow O(^3P) + O_2(X^3\Sigma_g^-) \quad (2c)$$

The NASA/JPL[9] has suggested that the deactivation of O(^{1}D) atoms by O_2 leads to production of $O_2(b^1\Sigma_g^+)$ by the energy exchange process 2a with an efficiency of 80 ± 20%, which is based on many experimental studies.[11−14] This process is thought to be a major source of $O_2(b^1\Sigma_g^+)$ in the atmosphere. The formation of $O_2(a^1\Delta_g)$ by the process 2b should be of minor importance. Izod and Wayne[15] found that the efficiency of reaction 2b is <1/30. Snelling[13] has estimated the rate of production of vibrationally excited O_2 ($X^3\Sigma_g^-$, v″), k(v″ = 13) = 2.3×10^{-13} cm^3 molecule^{-1} s^{-1} and k(v″ = 14) = 7×10^{-14} cm^3 molecule^{-1} s^{-1}, and has concluded that quenching reaction 2c is a minor process since the total rate of reaction 2c is 4.0×10^{-11} cm^3 molecule^{-1} s^{-1}.

2. Experiment

The experimental apparatus was the same as that used in our earlier work.[2,5] The translationally hot O(^{1}D) atoms were generated by the photodissociation of N_2O at 193 nm using an excimer laser operated with the ArF mode. The O(^{1}D) photofragments from N_2O photolysis were directly detected by a VUV laser-induced fluorescence (LIF) technique for the $3s^1D^\circ - 2p^1D$ transition at 115.22 nm, which was generated by phase-matched frequency tripling in xenon using a dye laser pumped by a XeCl excimer laser. The O(^3P_j) atoms produced by reaction 2 were probed for the $3s^3S^\circ - 2p^3P_j$ transition at 130.22 nm for $j = 2$, 130.48 nm for $j = 1$, and 130.60 nm for $j = 0$, respectively. The VUV laser around 130 nm was generated by four-wave difference mixing in krypton gas,[16] using two dye lasers pumped by the XeCl excimer laser. A part of the VUV light was reflected by a LiF window into a photoionization cell containing nitric oxide gas to measure the VUV laser intensity. The fluorescence of the O(^{1}D) and O(^3P_j) atoms was detected by a solar-blind photomultiplier tube. The output from the photomultiplier was preamplified and sampled by a gated integrator. In the Doppler profile measurements, the dissociation laser was polarized by a pile-of-plates polarizer. The delay time between the photolysis and probe laser was set to 50 ns − 20 μs with a jitter of less than 10 ns, which was controlled by a pulse generator. The reaction chamber (80 × 80 × 80 mm) was evacuated by a rotary pump (330 L/min) through a liquid N_2 trap. The pressure in the chamber was measured by a capacitance manometer. The gas mixture N_2O/O_2 flowed slowly through the reaction chamber. O_2 and N_2O gases were obtained commercially (ultrapure grade, >99.999%) and used without further purification.

3. Results and Discussion

3.1. Doppler Profiles of O(^{1}D). The hot O(^{1}D) atoms generated by the photodissociation of N_2O molecules at 193 nm are translationally relaxed by collisions with O_2 molecules (process 1). In this study, we measured Doppler profiles for O(^{1}D) at various delay times after the photodissociation to reveal the translational energy relaxation process 1. Typical Doppler profiles of the O(^{1}D) atoms at various delay times after the photodissociation are shown in Figure 1. The pressure of N_2O and O_2 was 5 mTorr and 1.0 Torr, respectively. By scanning the VUV probe laser wavelength around the resonance line of O(^{1}D) at 115.2 nm, the profiles of fluorescence excitation spectra were measured. The resonance frequency of an O(^{1}D) atom exhibits a Doppler shift $\Delta\nu = \nu_0\, w/c$, where w (= $\mathbf{v}\cdot\boldsymbol{k}_p$) is the component of the atom's velocity $\mathbf{v}$ along the propagation direction of the probe laser $\boldsymbol{k}_p$, and ν_0 is the center frequency of the atomic transition. The probe laser beam propagated at right angles to the propagation direction of the dissociation laser $\boldsymbol{k}_d$. At each delay time of $t = 35 \sim 1000$ ns, the Doppler profiles were taken under two different optical geometries, $\boldsymbol{k}_p \parallel \mathbf{E}_d$ and $\boldsymbol{k}_p \perp \mathbf{E}_d$, where $\mathbf{E}_d$ is the polarization vector of the photolysis laser. Doppler spectra which are indicated as $t = 0$ in Figure 1 were actually measured at the time delay of 40 ns with only 5 mTorr of N_2O and without O_2 gas; these spectra could be regarded as those for the nascent O(^{1}D) atoms in the photodissociation of N_2O at 193 nm because the translational energy relaxation was negligible under those conditions. The Doppler profiles under collisionless conditions have wide widths and different shapes between the two configurations, which indicates that the nascent O(^{1}D) atoms have a large translational energy and a recoil anisotropy. The translational energy distribution and the recoil anisotropy in the photodissociation of N_2O at 193 nm have been well studied, and the anisotropy parameter β has been reported to be ~0.5.[17−20] At long delay times, the Doppler profiles become close to that of thermalized atoms as shown in Figure 1.

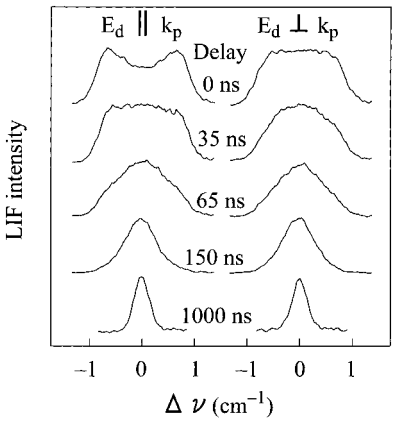

Figure 1. Doppler profiles for O(^{1}D) at various delay times between the photodissociation and probe laser pulses. The hot O(^{1}D) atoms were initially generated by the photodissociation of N_2O at 193 nm. Initial Doppler profiles (delay time 0 ns) were actually obtained without O_2 at a delay of 40 ns. The peak heights of the profiles are normalized. The pressures of N_2O and O_2 were 5 mTorr and 1.0 Torr, respectively. $\mathbf{E}_d$ is the direction of the electronic vector of the dissociation laser. $\boldsymbol{k}_p$ is the propagation direction of the probe laser.

Using the same analysis procedure as that in our previous study,[2,5] we calculated the velocity distributions of the O(^{1}D) atoms from the Doppler spectra. Figure 2 shows the time evolution of the translational energy distributions of the O(^{1}D) atoms in the laboratory (LAB) frame at delay times of 0, 65, 200, and 600 ns after the photodissociation of N_2O (5 m Torr) with 1.0 Torr of O_2. The open circles plotted in Figure 2 are the distributions revealed from the analysis of the Doppler profiles (Figure 1). For comparison, the Boltzmann distribution at 298 K is also shown by a smooth curve in Figure 2d. The distribution, even at the 600 ns delay time, is hotter than the Boltzmann distribution at 298 K. Figure 2 also shows the average translational energy, $\langle E_t \rangle$, as a function of the delay time. The $\langle E_t \rangle$ of the nascent O(^{1}D) atoms in the LAB frame was obtained to be 18.1 kcal mol^{-1}. The nascent translational energy distribution obtained is in good agreement with the result reported by Felder et al.,[18] which is shown by the smooth curve in Figure 2a.

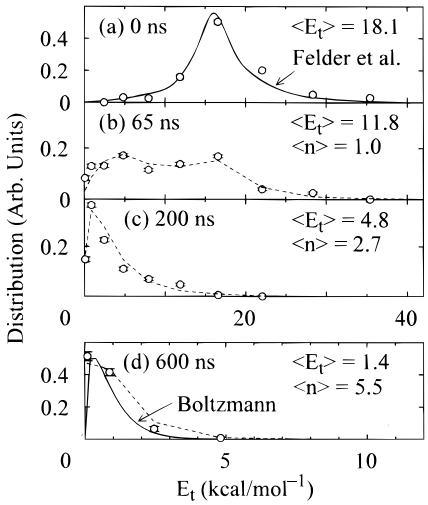

Figure 2. Time evolution of the translational energy distribution in the laboratory frame for hot O(^{1}D) after the photodissociation of N_2O. The pressure of N_2O and O_2 were 5 m Torr and 1.0 Torr, respectively. The distribution functions are obtained from the analysis of the Doppler profiles experimentally measured (Figure 1). $\langle E_t(t)\rangle$ is the average translational energy at each delay time. Vertical error bars are one-sigma deviations in the least-squares fitting calculations. The smooth curve shown in (a) indicates the experimental results presented by Felder et al.[18] The Boltzmann distribution at 298 K is also shown by a smooth curve in (d). Broken curves are the results of the Monte Carlo calculations with the hard-sphere collision diameter of 2.5 Å. $\langle n\rangle$ is the average collision number during each delay time (see text).

3.2. Simulation of the Translational Energy Relaxation Process. To simulate the experimental results of the translational energy relaxation process of hot O(^{1}D) atoms by collisions with O_2, we used an elastic hard-sphere collision model with a Monte Carlo method. The detail of the model was described in our previous paper.[2,5] Briefly, in the simulation the trajectory of each O(^{1}D) atom was calculated for sequential collisions until the time exceeds 1000 ns under the condition of an O_2 pressure of 1 Torr, that is, 1000 ns·Torr. All collision conditions for O(^{1}D) were generated randomly, with proper weight, and then the trajectory of the O(^{1}D) atom was calculated. After calculations of up to 5×10^4 trajectories, the translational energy distribution of O(^{1}D) in the LAB frame was obtained at each delay time up to 1000 ns·Torr. The simulations with the hard-sphere model reproduce well the experimental results obtained for the collisions of O(^{1}D) with O_2. Figure 3 shows the results of the model simulations (smooth curves) and the experiments (open circles) for the average translational energy of O(^{1}D) at various delays after the photodissociation of N_2O. The logarithm of $[\langle E_t(t)\rangle - \langle E_t^{th}\rangle]/[\langle E_t(0)\rangle - \langle E_t^{th}\rangle]$ is plotted versus delay time in Figure 3, where $\langle E_t(t)\rangle$ is the average translational energy of O(^{1}D) at delay time t as shown in Figure 2, $\langle E_t^{th}\rangle$ is the average thermal energy of the O(^{1}D) atoms at 298 K (0.89 kcal mol^{-1}), and $\langle E_t(0)\rangle$ is the average of the initial translational energy. The slope of the plots corresponds to the rate of the translational energy relaxation. The best-fit value of the hard-sphere collision diameter, d, is 2.5 ± 0.2 Å for $\langle E_t(0)\rangle = 18.1$ kcal mol^{-1}, as shown in Figure 3. This value is in good agreement with the value of 2.4 Å for $\langle E_t(0)\rangle = 9.8$ kcal mol^{-1}, which was reported by Matsumi et al.[5]

The translational energy distributions for O(^{1}D) at various delay times are also well reproduced by the elastic hard-sphere model calculations. The broken lines in Figure 2b−d indicate the translational energy distributions simulated by the elastic hard-sphere collision model with $d = 2.5$ Å at each delay time. The average number of collisions suffered by each O(^{1}D) atom during the delay times after the photodissociation, $\langle n\rangle$, are also indicated in Figure 2.

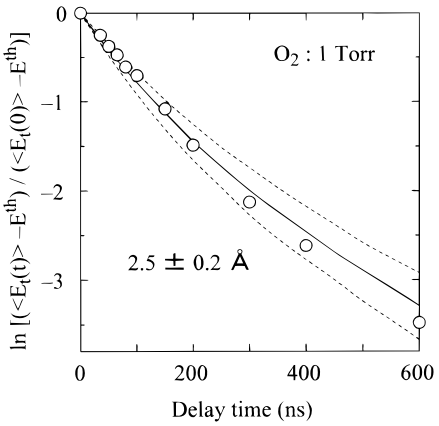

Figure 3. Time evolution of translational energies. The vertical scale is $\ln[\langle E_t(t)\rangle - \langle E_t^{th}\rangle]/[\langle E_t(0)\rangle - \langle E_t^{th}\rangle]$. $\langle E_t(t)\rangle$ is the average translational energy at delay time t. $\langle E_t^{th}\rangle$ is the average thermal translational energy at 298 K, that is, 0.89 kcal mol^{-1}. Slopes of these plots correspond to the speed relaxation rates of the translational energy. The source of the initial hot O(^{1}D) atoms was photodissociation of N_2O at 193 nm. The pressure of O_2 was 1.0 Torr. Smooth lines are the simulated results of the Monte Carlo calculations with the hard-sphere collision diameter of 2.5 with uncertainty of 0.2 Å (broken curve).

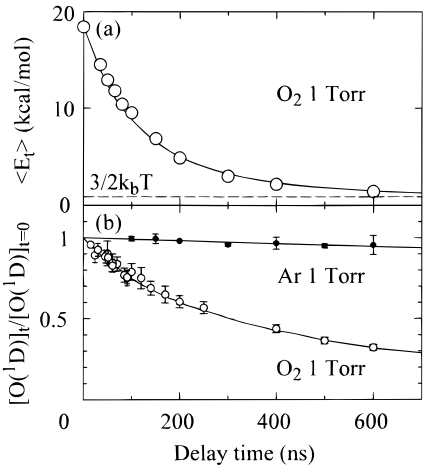

Figure 4. (a) Time evolution of the average translational energy, $\langle E_t\rangle$, for the O(^{1}D) atoms produced from the photodissociation of N_2O at 193 nm. The value of $\langle E_t\rangle$ at each delay time was obtained from the analysis of the Doppler profiles, which were taken under the conditions of 5 − 6 mTorr of N_2O and 1.0 Torr of O_2. The smooth curve is the result of the simulation with the hard-sphere collision diameter of 2.5 Å. The broken line indicates the thermal translational energy at 298 K, that is, 0.89 kcal mol^{-1}. (b) Time evolution of the concentration for the O(^{1}D) atoms (open circles) under the same experimental conditions as (a). The vertical scale is normalized by the initial O(^{1}D) concentration. For comparison, the concentration change with 1.0 Torr of Ar instead of O_2 is also plotted (filled circles). The smooth curve is the result of the simulation (see text).

3.3. Electronic Quenching Process. Figure 4a shows the time evolution of the average translational energy, $\langle E_t(t)\rangle$, versus delay time after the photodissociation of N_2O at 193 nm. To study the electronic quenching process 2, we measured the relative concentration of O(^{1}D) at various delay times after the photodissociation. By integrating the Doppler profile at each delay time and then normalizing with the initial concentration, we obtained the decay of the concentration for O(^{1}D) atoms (open circles) by the electronic quenching process 2 as shown in Figure 4b. The decay curve in Figure 4b was taken under the same experimental conditions with the energy plots in Figure 4a. The

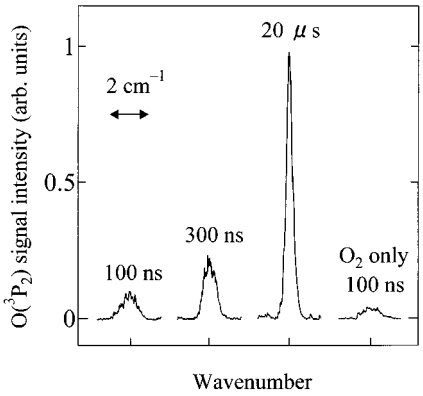

Figure 5. Excitation spectra of $O(^3P_2)$ at delay times of 100 ns, 300ns, and 20 μs after the photodissociation of N_2O at 193 nm. The pressures of O_2 and N_2O were 300 mTorr and 3 mTorr, respectively. At 20 μs, almost 100% of the $O(^1D)$ atoms were converted to $O(^3P_j)$. The excitation spectrum of $O(^3P_2)$ with only O_2 and without N_2O gas at a 100-ns delay time is also shown. The contribution of $O(^3P_j)$ atoms from the photodissociation of O_2 at 193 nm was less than 13% of the total signal at 20 μs, even when the N_2O pressure was as low as 3 mTorr.

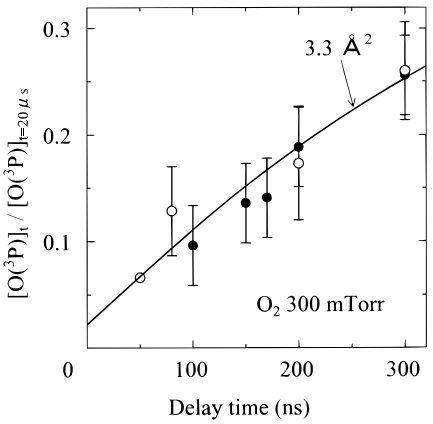

Figure 6. Plots of $O(^3P_j)$ concentration versus delay time after the photodissociation of N_2O at 193 nm, when the pressure of O_2 was 300 mTorr. The vertical axis is the relative $O(^3P_j)$ concentration normalized with that at a 20-μs delay time. The contributions of $O(^3P_j)$ atoms from the O_2 photodissociation are already subtracted. Open and solid circles show the experimental data obtained under the different conditions of N_2O/O_2 gas mixture ratio, 1% and 8%, respectively. Smooth curves are the results of the simulation with the reaction cross section of 3.3 Å^2 for $O(^1D) + O_2 \rightarrow O(^3P_j) + O_2$. The uncertainty of the reaction cross section by the simulation is 0.7 Å^2.

decay curve of the $O(^1D)$ concentration at $t = 0 - 50$ ns was estimated from the increase of the $O(^3P_j)$ concentration produced by process 2, which will be described later. For comparison, the change of $O(^1D)$ concentration with 1.0 Torr of Ar bath gas instead of O_2 is also plotted in Figure 4b (filled circles). The quenching rate constant for $O(^1D) + Ar$ at 300 K is about 20 times as small as that for $O(^1D) + O_2$.[21−24]

Comparing Figure 4a with 4b, it should be noted that about 60% of hot $O(^1D)$ atoms are electronically quenched to $O(^3P)$ atoms before the entire thermalization of the hot $O(^1D)$ atoms is completed in a gaseous mixture with O_2, when the initial $\langle E_t \rangle$ of the $O(^1D)$ atoms is 18.1 kcal mol^{-1}. From the same type of experiments, Matsumi and Chowdhury[2] found that the translational energy relaxation rate of $O(^1D)$ by collisions with N_2 was not fast compared with the electronic quenching by N_2. They have suggested that the steady-state distribution of the $O(^1D)$ translational energy in the upper stratosphere is superthermal and that the populations at large translational energies are higher than those estimated from an equilibrated condition with the ambient air, since translationally hot $O(^1D)$ atoms are produced by the photodissociation of O_3 and O_2. Although the collision frequency of $O(^1D)$ atoms with O_2 in the atmosphere is lower than that with N_2 due to the smaller abundance, our results on the collisions with O_2 reinforce their suggestion.

3.4. Reaction Cross Section of the Electronic Quenching Process. As shown in Figure 4a, the translational energies of the $O(^1D)$ atoms are large at short delays after the photodissociation. Therefore, the initial decay of the $O(^1D)$ concentration and the initial rise of the $O(^3P_j)$ concentration contain information about the reaction cross sections for the reaction 2 at high collision energies. We measured the small rise of the concentration of the $O(^3P_j)$ atoms produced by quenching process 2 after the photodissociation of N_2O at 193 nm, since it was difficult to measure a few percent decreases in the concentration of $O(^1D)$ at short delays precisely. Figure 5 shows typical VUV LIF excitation spectra of the $O(^3P_2)$ atoms around 130 nm at delay times of 100 ns, 300 ns, and 20 μs after the photodissociation of N_2O at 193 nm. At 20 μs after the photodissociation of N_2O, almost 100% of $O(^1D)$ atoms were converted to $O(^3P_j)$ atoms. By normalizing the area under the peak in the excitation spectrum at each delay time with that at 20 μs, we obtained the relative concentration of the $O(^3P_j)$ atoms. The relative concentration of $O(^3P_j)$ versus delay time is plotted in Figure 6, when the pressure of O_2 was 300 mTorr and the concentration of N_2O was $1 - 8\%$ of O_2. The j-branching among the fine-structure levels of $O(^3P_j)$ is also taken into account. The vertical scale of Figure 6 is the relative concentration, $[O(^3P_j)]_t/[O(^3P_j)]_{20\mu s}$, where $[O(^3P_j)]_t$ is the concentration at delay time t and $[O(^3P_j)]_{20\mu s}$ is that at 20 μs. A small amount of $O(^3P_j)$ atoms are produced by the photodissociation of O_2 at 193 nm in addition to the electronic quenching of $O(^1D)$ atoms. Figure 5 also shows the excitation spectra of $O(^3P_j)$ at 100 ns delay time after the photodissociation with only O_2 and without N_2O gas. The contribution of $O(^3P_j)$ atoms from the photodissociation of O_2 was less than 13% of the total signal at 20 μs, even when the N_2O pressure was as low as 3 mTorr. The $O(^1D)$ atoms also react with N_2O molecules as well as O_2. However, the removal of $O(^1D)$ atoms by the reaction with N_2O could be regarded as negligibly small since the partial pressure of N_2O was much smaller than that of O_2 in our experiments. Actually, the rise of the $O(^3P_j)$ relative concentration is independent of the N_2O partial pressure ($1 - 8\%$ of O_2) within experimental errors, as shown in Figure 6.

The smooth curve in Figure 6 (also Figure 4b) shows the results of the simulation, in which both speed relaxation and the reactive removal of $O(^1D)$ by collisions with O_2, that is, processes 1 and 2, are taken into account. The reaction cross section of the electronic quenching processes 2, σ_r, was taken as a fitting parameter. The best fit value of σ_r is 3.3 ± 0.7 Å^2. We calculated the collision energy distributions using the elastic hard-sphere collision model described above. Distributions of the collision energy between $O(^1D)$ and O_2 in the center-of-mass frame during the various collision time periods from the photodissociation of N_2O in 300 mTorr of O_2 are shown in Figure 7; the distributions were calculated under the conditions that the hard-sphere diameter for the translational energy relaxation (process 1) is 2.5 Å and the initial translational energy distribution of $O(^1D)$ in the LAB frame is that for the photodissociation of N_2O at 193 nm (see Figure 2). Due to the initial distribution of the $O(^1D)$ translational energy in the photodissociation of N_2O and also to the thermal velocity of the O_2 molecules, the distribution of the collision energy is broad even for the time period of $0 - 50$ ns. The distribution for the time period of $0 - 300$ ns is a little broader than that for $0 -$

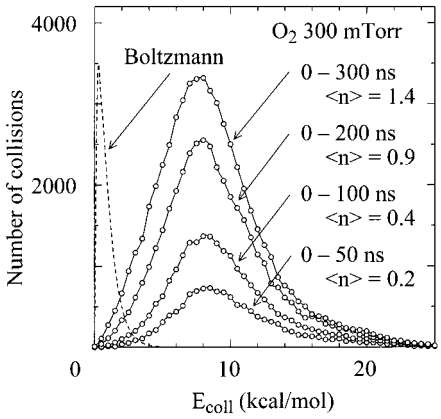

Figure 7. Distributions of the collision energy between $O(^1D)$ and O_2 in the center-of-mass frame during various delay time periods after the photodissociation of N_2O; distributions are the results of the simulation with the hard-sphere collision diameter of 2.5 Å. In the simulation, 50,000 trajectories of $O(^1D)$ atoms were calculated. The pressure of O_2 was 300 mTorr. $\langle n \rangle$ is the average collision time during each collision time. For comparison, the Boltzmann distribution at 298 K, which is not normalized, is also plotted (broken curve).

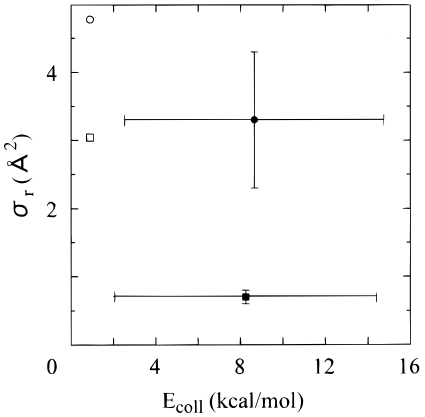

Figure 8. Collision energy dependence of the reaction cross section, σ_r, for $O(^1D) + O_2 \rightarrow O(^3P_j) + O_2$. Solid circle is our experimental result. Open circle is the average cross section at 298 K that is calculated with $k = \langle v \rangle \cdot \sigma_r$, where k is the reaction rate constant, 4.0×10^{-11} cm^3 molecule^{-1} s^{-1}, and $\langle v \rangle$ is the average relative speed between $O(^1D)$ and O_2 at 298 K. For comparison, the collision energy dependence of the σ_r for $O(^1D) + N_2 \rightarrow O(^3P_j) + N_2$ is also shown (squares) (ref 2).

50 ns, which is due to the multiple collisions of $O(^1D)$ after the photodissociation. From these simulations, the center-of-mass collision energy, E_{coll}, was defined as 8.7 ± 6 kcal mol^{-1} for the collision period of $0 - 300$ ns at 300 mTorr of O_2.

Figure 8 shows the collision energy dependence of σ_r for $O(^1D) + O_2$. The solid circle with error bars plotted in Figure 8 is the result obtained in this study. The size of the horizontal error bar is large, which is mainly due to the translational energy distribution of the nascent $O(^1D)$ produced by the photodissociation of N_2O, as shown in Figure 7. The value for the thermal collision energy at 298 K ($E_{coll} = 0.89$ kcal mol^{-1}) is also plotted in Figure 8 (open circle); this value was estimated from the reaction rate constant at 298 K, 4.0×10^{-11} cm^3 molecule^{-1} s^{-1} (ref 9). The σ_r of 3.3 ± 0.7 Å^2 at the high collision energy of 8.7 ± 6 kcal mol^{-1} is a little smaller than that at the thermal collision energy at 298 K (4.8 Å^2).

3.5. Dynamics of the Quenching Reaction. The quenching rate constant by O_2 at room temperature is 4.0×10^{-11} cm^3 molecule^{-1} s^{-1} (ref 9), which is smaller than the gas kinetic collision frequency rate. The temperature dependence of the quenching rate constant by O_2 shows a small negative or no activation energy, $k(T) = 3.2 \times 10^{-11} \exp[(70 \pm 100)/RT]$ (ref 9). The temperature dependence of the rate constant is consistent with our results of the small decrease of σ_r with an increase of the E_{coll}, as shown in Figure 8. This suggests that the entrance potential of $O(^1D) + O_2$ ($X^3\Sigma_g^-$) is attractive and has no barrier on the reaction pathway. In the main reaction process 2a, both the entrance surface of $O(^1D) + O_2(X^3\Sigma_g^-)$ and the exit surface of $O(^3P) + O_2(b^1\Sigma_g^+)$ correlate to the triplet electronic states of O_3 molecule. Banichevich and Peyerimhoff[25] have presented ab initio calculations of the potential surfaces of the triplet state of O_3. However, they calculated the potential surfaces of low-lying states that correlate to $O(^3P) + O_2(X^3\Sigma_g^-)$ and $O(^3P) + O_2(a^1\Delta_g)$. The triplet potential surfaces, which take part in this quenching reaction, have not been investigated theoretically. The reactant combination of $O(^1D) + O_2$ ($X^3\Sigma_g^-$) correlates to five triplet states of O_3. At least one of them probably has an attractive potential along the $O-O_2$ bond length and leads to the quenching reaction. The others may have repulsive potential surfaces and lead to nonreactive scattering processes.

Matsumi and Chowdhury[2] presented the energy dependence of the cross section for the observed quenching reaction by N_2,

$$O(^1D) + N_2(X^1\Sigma_g^+) \rightarrow O(^3P) + N_2(X^1\Sigma_g^+, v, J) \qquad (3)$$

using the same experimental technique as this study. Their results for the quenching by N_2 are also plotted by squares in Figure 8 for comparison. The σ_r by N_2 at the high collision energy of 8.3 ± 6 kcal mol^{-1} was found to be 0.7 ± 0.1 Å^2, which is about four times smaller than that at the thermal collision energy at 298 K. Their experimental results are in good agreement with the results of the trajectory calculations on ab initio potentials by Tachikawa et al.[7] and the statistical calculations by Zahr et al.[26] The entrance potential of the quenching reaction 3 by N_2 has singlet spin-multiplicity, whereas the exit potential is triplet. Therefore, the quenching process by N_2 is spin-forbidden. The spin-orbit interaction is responsible for the surface change from the singlet to the triplet potentials during quenching reaction 3. The spin-orbit interaction in the N_2O complex has small strength, since the N_2O complex consists of only light atoms. The transition probabilities at the seams between the singlet and triplet potentials should be small. The quenching rate constant for reaction 3 at room temperature is 2.6×10^{-11} cm^3 molecule^{-1} s^{-1} (ref 9), which is a little smaller than that for reaction 2. The entrance potential for reaction 3 should be strongly attractive, since the $O(^1D) + N_2(X^1\Sigma^+_g)$ potential leads to the ground electronic state of the highly stable N_2O molecule. The strong attractive potential results in long lifetimes of the singlet complex of N_2O. The trajectories of the collision complex on the singlet surface cross the seams to the triplet surface many times during their lifetimes. This mechanism can explain the relatively fast rate for the quenching reaction of $O(^1D)$ with N_2 despite the spin-forbidden nature.[27] At higher collision energies, the lifetime of the complex becomes shorter and there is thus less chance to cross the seams between the singlet and triplet surfaces. This is responsible for the large decrease of σ_r with the increase of the E_{coll} for $O(^1D) + N_2$.[26]

On the other hand, the main process (reaction 2a) of the quenching reaction of $O(^1D)$ by O_2 is spin-allowed. Compared with the quenching reaction by N_2, the transition probability at the seams between the two surfaces is expected to be large in the quenching reaction by O_2 due to the spin-allowed character of the interaction. If the surface hopping takes place at every crossing at the seams, the reaction probability does not depend on the lifetime of the complex. Here, we assume that all of the

trajectories switch their surfaces to O(^{3}P) + O$_2$(b$^1\Sigma_g^+$) after the formation of collision complex. In reactions that have entrance potential surfaces with only attractive forces, the cross section of complex formation is determined by the effective potential resulting from addition of the attractive potential and centrifugal forces.[26,28] If the attractive force is based on dipole−induced dipole and/or dispersion interactions, that is, $V(r) = -c/r$,[6] the cross section is proportional to $E_{coll}^{-1/3}$, where c is an interaction constant and r is the distance between the reactants. From our experimental study for O(^{1}D) + O$_2$ collision, the ratio of the quenching cross sections of $\sigma_r(\langle E_{coll}\rangle = 8.7$ kcal/mol)/$\sigma_r(\langle E_{coll}\rangle = 0.89$ kcal/mol) is 0.69 ± 0.15. With the $E_{coll}^{-1/3}$ dependence, the ratio is calculated to be 0.47. The difference between the experimental result and the theoretical one may be due to a deviation of the attractive potential from the $V(r) = -c/r^6$ shape and/or the reaction probability at the seams. Thus, the experimentally obtained collision energy dependence can be explained simply by the centrifugal forces on the entrance attractive potential.

Acknowledgment. This work was partly supported by grants-in-aid from the Ministry of Education, Science, and Culture of Japan. Y.M. is indebted to the Iwatani Foundation. K.T. wishes to thank the Asahi Breweries Foundation for financial support. This work was partly supported by the research project, "Computational Chemistry for Atmospheric Environmental Molecule" under Research and Development Applying Advance Computational Science and Technology administrated by Japan Science and Technology Corporation (ACT-JST).

References and Notes

(1) Wayne, R. P. *Chemistry of Atmospheres*, 2nd ed.; Oxford University Press: New York, 1991.
(2) Matsumi, Y.; Chowdhury, A. M. S. *J. Chem. Phys.* **1996**, *104*, 7036.
(3) Cline, J. I.; Taajes, C. A.; Leone, S. R. *J. Chem. Phys.* **1990**, *93*, 6543.
(4) Nan, G.; Houston, P. L. *J. Chem. Phys.* **1992**, *97*, 7865.
(5) Matsumi, Y.; Shamsuddin, S. M.; Sato, Y.; Kawasaki, M. J. *Chem. Phys.* **1994**, *101*, 9610.
(6) Tachikawa, H.; Hamabayashi, T.; Yoshida, H. *J. Phys. Chem.* **1995**, *99*, 16630.
(7) Tachikawa, H.; Ohnishi, K.; Hamabayashi, T.; Yoshida, H. *J. Phys. Chem.* **1997**, *101*, 2229.
(8) Balakrishnan, N.; Kharchenko, V.; Dalgarno, A. *J. Phys. Chem.* **1999**, *103*, 3999.
(9) DeMore, W. B.; Sander, S. P.; Howard, C. J.; Ravishankara, A. R.; Golden, D. M.; Kolb, C. E.; Hampson, R. F.; Kurylo, M. J.; Molina, M. J. *Chemical Kinetics and Photochemical Data for use in Stratospheric Modeling*; No. 12; JPL Publication 97-4: Pasadena, CA, 1997.
(10) Streit, G. E.; Howard, C. J.; Schmeltekopf, A. L.; Davidson, J. A.; Schiff, H. I. *J. Chem. Phys.* **1976**, *65*, 4761.
(11) Noxon, J. F. *J. Chem. Phys.* **1970**, *52*, 1852.
(12) Biedenkapp, D.; Bair, E. J. *J. Chem. Phys.* **1970**, *52*, 6119.
(13) Snelling, D. R. *Can. J. Chem.* **1974**, *52*, 257.
(14) Lee, L. C.; Slanger, T. G. *J. Chem. Phys.* **1978**, *69*, 4053.
(15) Izod, T. J. P.; Wayne, R. P. *Proc. R. Soc. London* **1968**, *308*, 81.
(16) Hilbig, R.; Hilber, G.; Wallenstein, R. *Appl. Phys.* **1986**, *41*, 225.
(17) Springsteen, L. L.; Satyapal, S.; Matsumi, Y.; Dobeck, L. M.; Houston, P. L. *J. Phys. Chem.* **1993**, *97*, 7239.
(18) Felder, P.; Haas, B.-M.; Huber, J. R. *Chem. Phys. Lett.* **1991**, *186*, 177.
(19) Suzuki, T.; Katayanagi, H.; Mo, Y.; Tonokura, K. *Chem. Phys. Lett.* **1996**, *256*, 90.
(20) Chang, B.; Hoetzlein, R. C.; Mueller, J. A.; Geiser, J. D.; Houston, P. L. *Rev. Sci. Instrum.* **1998**, *69*, 1665.
(21) Stief, L. J.; Payne, W. A.; Klemm, R. B. *J. Chem. Phys.* **1975**, *62*, 4000.
(22) Heidner, R. F., III; Husain, D. *Int. J. Chem. Kinet.* **1974**, *6*, 77.
(23) Cohen, J. S.; Wadt, W. R.; Hay, P. J. *J. Chem. Phys.* **1979**, *71*, 2955.
(24) Davidson, J. A.; Schiff, H. I.; Brown, T. J.; Streit, G. E.; Howard, C. J. *J. Chem. Phys.* **1978**, *69*, 1213.
(25) Banichevich, A.; Peyerimhoff, S. D. *Chem. Phys.* **1993**, *178*, 155.
(26) Zahr, G. E.; Preston, R. K.; Miller, W. H. *J. Chem. Phys.* **1975**, *62*, 1127.
(27) Tully, J. C. *J. Chem. Phys.* **1974**, *61*, 61.
(28) Pechukas, P.; Light, J. C.; Rankin, C. *J. Chem. Phys.* **1966**, *44*, 794.